Journal of Materials Chemistry C

ROYAL SOCIETY OF CHEMISTRY

PAPER

View Article Online
View Journal | View Issue



Cite this: J. Mater. Chem. C, 2023, 11, 5646

# A heavily doped D–D′-type polymer with metal-like carrier transport *via* hybrid doping†

Ayushi Tripathi,[a] Yoonjoo Lee,[a] Changhwa Jung,[b] Soohyun Kim,[b] Soonyong Lee,[a] Woojin Choi,[b] Chaeyeon Park,[a] Young Wan Kwon,[c] Hyunjung Lee *[b] and Han Young Woo *[a]

Received 21st January 2023,
Accepted 30th March 2023

DOI: 10.1039/d3tc00260h

rsc.li/materials-c

A new donor–donor (D–D′)-type polymer (PIDTSCDTS) based on electron-rich indacenodithiophene (IDT) and cyclopentadithiophene (CDT) moieties is synthesized with extended π-conjugation and pronounced chain planarity through substitution with $sp^2$-hybridized alkenyl side chains. Its thermoelectric (TE) properties are studied in detail depending on the doping methods: sequential doping (SqD), solution-mixed doping (MxD), and hybrid doping (HyD) with $AuCl_3$ and $FeCl_3$ as p-dopants. The carrier generation and transport depend strongly on the doping method. A higher conductivity ($\sigma$) of up to ~500 S $cm^{-1}$ is achieved using HyD (compared with other methods) owing to the significantly higher (bi)polaron generation (of up to ~$10^{21}$ $cm^{-3}$) by doping both the amorphous and crystalline regions. Analyzing the relationship between the Seebeck coefficient ($S$) and the conductivity ($\sigma$) based on the Kang–Snyder model, metal-like carrier transport is observed for polymers obtained *via* SqD and HyD, which has been barely reported in organic TE polymers. The higher transport coefficient ($\sigma_{E0}$) in the HyD films reduces the $S$–$\sigma$ trade-off relation, leading to a larger maximum power factor, $PF_{max}$, of ~40 μW $m^{-1}$ $K^{-2}$ with simultaneously enhanced $\sigma$ and $S$ values compared with SqD films (16 μW $m^{-1}$ $K^{-2}$). To further optimize the TE properties, the degenerate doping and band-like carrier transport with maximizing the $\sigma_{E0}$ need to be carefully considered for the molecular design and doping process.



## 1. Introduction

Organic thermoelectric (TE) polymers have attracted considerable attention owing to their unique properties, such as the facile tuning of their molecular structures and electrical properties, their low intrinsic thermal conductivity ($\kappa$), their light weight, mechanical flexibility, and room-temperature solution processability on flexible substrates.[1–5] Waste heat at temperatures below ~200 °C accounts for approximately 60% of the total amount of unrecovered waste heat each year,[6] and such low-temperature heat waste can be converted to electricity more efficiently by organic TE materials compared with their inorganic counterparts.[7–9]

The efficacy of TE power conversion is analyzed in terms of the dimensionless figure of merit, $ZT = S^2\sigma T/\kappa$ or power factor (PF, *i.e.*, $S^2\sigma$), where $\sigma$, $S$, and $T$ are the electrical conductivity, Seebeck coefficient, and absolute temperature, respectively.[10–12] To maximize the $ZT$ value, both $\sigma$ and $S$ need to be increased, while $\kappa$ should be decreased; however, $\sigma$ and $S$ have a trade-off relationship ($\sigma$ increases but $S$ decreases with increasing carrier concentration) and all the TE parameters are strongly dependent on the carrier concentration.[13–16] The electrical conductivity ($\sigma = ne\mu$; $n$ = carrier concentration; $e$ = electron charge; $\mu$ = carrier mobility) depends on the carrier concentration and its mobility. To mitigate the $S$–$\sigma$ trade-off relation, increasing the $\sigma$ by controlling the carrier transport ability also needs to be considered *via* the morphological control of the doped state. Therefore, molecular design for facile doping (to achieve a degenerate doping) with strong interchain crystalline packing is needed. It is also necessary to tailor the doping method and conditions depending on the specific molecular structure to efficiently generate (bi)polarons without disruption of the (semi)crystalline morphology of pristine films. For example, the widely utilized doping technique of solution-mixed doping (MxD), which is a simple one-step process that involves mixing host polymers and dopants in solution, often induces aggregation and phase separation at high dopant concentrations. This ultimately leads to a poor film morphology and deteriorates the charge carrier transport. As a result, in MxD polymeric systems, the charge transport is often governed by impurity scattering with a poor $\mu$. The carrier transport in doped polymers is much more complex

[a] Department of Chemistry, College of Science, Korea University, Seoul 02841, Republic of Korea. E-mail: hywoo@korea.ac.kr
[b] School of Materials Science and Engineering, Kookmin University, Seoul, 02707, Republic of Korea. E-mail: hyunjung@kookmin.ac.kr
[c] KU-KIST Graduate School of Converging Science and Technology, Korea University, Seoul 02841, Republic of Korea

† Electronic supplementary information (ESI) available. See DOI: https://doi.org/10.1039/d3tc00260h

than that in undoped systems because of the energetic and structural disorders induced by doping.[17–20] Therefore, fine modulation of the carrier generation and transport in doped states is required.[21,22] The carrier generation, transport, and resulting TE properties are strongly dependent on both the molecular design (or structure) and the specific doping method, which have received little attention so far and few systematic studies have been reported. Fundamental studies on how to achieve degenerate doping with metal-like carrier transport are necessary to further optimize organic TE devices.

In this contribution, we synthesized a new donor–donor (D–D′)-type polymer (PIDTSCDTS) based on two electron-rich p-type building blocks of indacenodithiophene (IDT) and cyclopentadithiophene (CDT). The D–D′-type molecular design with alkenyl side-chains was considered to improve the chain planarity and interchain crystalline packing as well as efficient p-doping. An in-depth study on $\sigma$, $n$, $\mu$, the morphology, the carrier transport, and the resulting TE characteristics was conducted using three different doping methods: solution-mixed doping (MxD), sequential doping (SqD), and hybrid doping (HyD). Two different types of Lewis acid dopant, $AuCl_3$ and $FeCl_3$, were employed for molecular doping. The $\sigma$ of PIDTSCDTS could be successfully optimized up to $\sim$500 S cm$^{-1}$ *via* degenerate doping utilizing the HyD method. The metal–insulator–semiconductor (MIS) capacitance measurements suggest that the origin of the higher $\sigma$ value is the significantly larger $n$ in the HyD films (compared with MxD and SqD films) with efficient doping in both amorphous and crystalline regions. UV-vis-NIR absorption, electron paramagnetic resonance (EPR) and corresponding $\sigma$ measurements suggested that the facile polaron to bipolaron transition in the HyD and SqD films and the resulting bipolaronic species are the main charge carriers in the heavily doped state. In addition, the charge transport behavior in doped-films depending on the doping methods was investigated through $S$–$\sigma$ analysis using the Kang–Snyder model. The SqD and HyD films exhibited metal-like charge transport and a transport parameter ($s$) of $s$ = 1, which has barely been reported except for poly(3,4-ethylenedioxythiophene) (PEDOT) derivatives and some highly crystalline polymers.[23,24] Furthermore, the higher transport coefficient ($\sigma_{E0}$) in HyD-PIDTSCDTS reduced the sacrifice of $S$ with increasing $\sigma$, which resulted in the highest PF of $\sim$40 μW m$^{-1}$ K$^{-2}$. Our systematic study may provide insight into further optimization of TE properties by inducing a heavily doped state with metallic transport and a high $\sigma_{E0}$.

## 2. Results and discussion

Fig. 1(a) shows the synthetic route to the donor–donor (D–D′)-type polymer PIDTSCDTS. 4,9-Bis(bis(hexylthio)methylene)-4,9-dihydro-*s*-indaceno[1,2-*b*:5,6-*b*′]dithiophene-2,7-diyl-bis(trimethylstannane) (**M1**) and 4-(bis((2-hexyldecyl)thio)methylene)-2,6-dibromo-4*H*-cyclopenta[2,1-*b*:3,4-*b*′]dithiophene (**M2**) were synthesized according to previously reported methods[25,26] Stille coupling

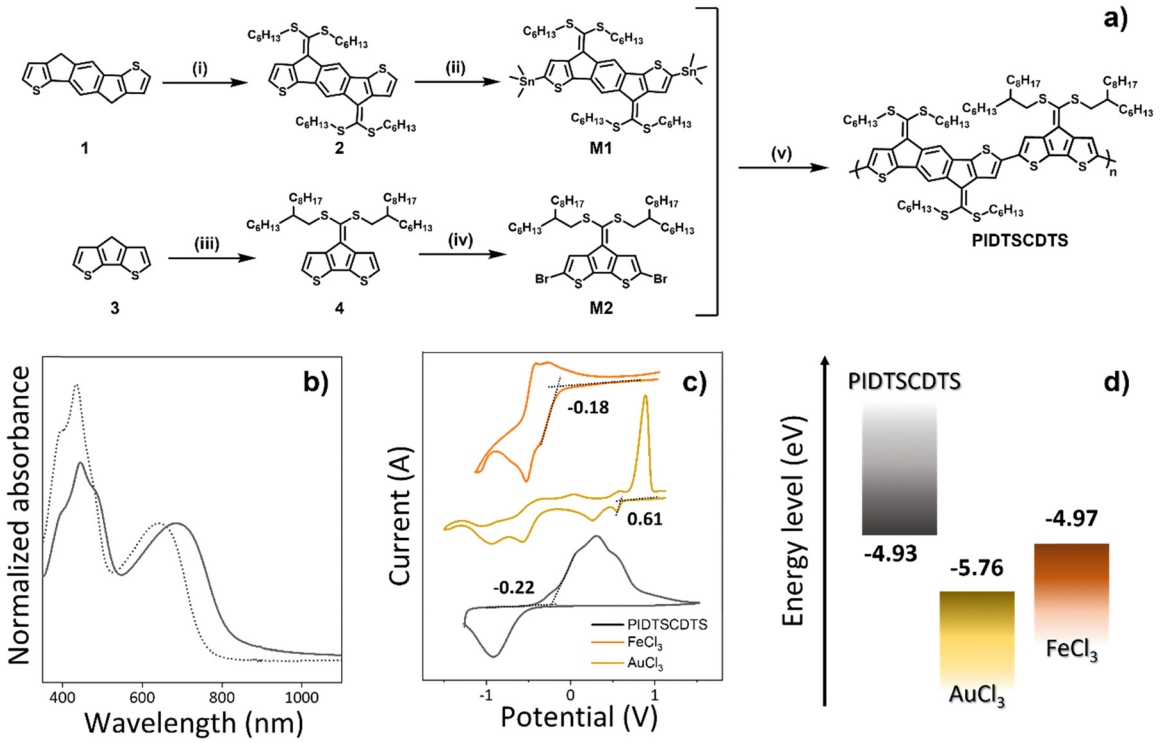


Fig. 1 (a) Synthetic route to PIDTSCDTS. *Reagents and conditions*: (i) *t*-BuOK, $CS_2$, bromohexane, room temperature (RT), dimethyl sulfoxide (DMSO); (ii) 2,2,6,6-tetramethylpiperidine, *n*-BuLi, tetrahydrofuran, $Me_3SnCl$; (iii) *t*-BuONa, $CS_2$, 2-hexyldecyl bromide, RT, DMSO; (iv) *N*-bromosuccinimide, *N*,*N*-dimethylformamide, 0 °C; (v) $Pd_2(dba)_3$, P(*o*-tol)$_3$, toluene, 100 °C, 24 h. (b) UV-vis-NIR absorption spectra in chloroform (dotted) and as a thin film (solid). (c) Cyclic voltammograms and (d) energy-level diagram of PIDTSCDTS and the dopants.

of the stannylated **M1** and brominated **M2** was performed to produce PIDTSCDTS (93% yield) using tris(dibenzylideneacetone)dipalladium ($Pd_2(dba)_3$) and P(*o*-tol)$_3$ as the catalyst system in toluene. To ensure sufficient solubility, a branched alkyl chain was employed on one of the monomers, whereas a linear alkyl chain on the other monomer was selected to minimize packing disruption. The polymer was purified *via* sequential Soxhlet extraction with methanol, acetone, and hexane. We designed the polymer carefully by considering an efficient charge generation (to achieve a degenerate doping with high $n$) and transport (high $\mu$). The electron-sufficient D–D′-type design motif was adopted by considering its facile p-doping together with effective stabilization of the positive charge carriers (of (bi)polarons) *via* extended delocalization, as reported in our previous study.[26] The sp$^2$-hybridized alkenyl side-chains were substituted onto a polymer chain, which enhances the chain planarity with extended π-conjugation and superior interchain packing *via* sulfur–sulfur (S–S) chalcogen interactions.[25] The number-averaged molecular weight ($M_n$) and the dispersity ($Đ$) of the polymer were measured as 68 kDa and 3.3, respectively, using gel permeation chromatography (relative to polystyrene standards) with *o*-dichlorobenzene (*o*-DCB) eluent at 80 °C. The molecular structures of the intermediates, monomers, and PIDTSCDTS were confirmed *via* $^1$H/$^{13}$C NMR spectroscopy and matrix-assisted laser desorption ionization-time of flight (MALDI-TOF) mass spectrometry, showing good agreement with the proposed structures (ESI†). Thermogravimetric analysis (TGA) showed the good thermal stability of PIDTSCDTS, with a decomposition temperature ($T_d$) of 291 °C at 5% weight loss (Fig. S1a, ESI†). Differential scanning calorimetry (DSC) measurements showed no phase transition in the range of 25–250 °C (Fig. S1b, ESI†).

The UV-vis-NIR absorption spectra of PIDTSCDTS measured in chloroform and as thin films are shown in Fig. 1(b). The absorption maxima for the π–π* transition was measured at $\lambda_{abs}$ = 435 nm in chloroform and $\lambda_{abs}$ = 442 nm in the film, and the intramolecular charge transfer (ICT) band was measured at $\lambda_{abs}$ = 642 nm in chloroform and $\lambda_{abs}$ = 685 nm in the film. The spectrum in the film was slightly red-shifted compared with that in solution, implying interchain aggregation in the solid film. The absorption edge ($\lambda_{edge}$) of PIDTSCDTS was at 823 nm in the film, corresponding to an optical bandgap ($E_g^{opt}$) of 1.27 eV. Cyclic voltammetry (CV) measurements were carried out in 0.1 M tetrabutylammonium tetrafluoroborate ($Bu_4NBF_4$) in acetonitrile using a conventional three-electrode system: Ag/$AgNO_3$ acted as the reference electrode, a platinum wire was the counter electrode, and a platinum electrode coated with a thin polymer film was the working electrode. The highest occupied molecular orbital (HOMO) energy level of the polymer was determined to be −4.93 eV based on the oxidation onset potential relative to an internal standard of the ferrocene/ferrocenium couple ($Fc/Fc^+$) (Fig. 1c). The lowest unoccupied molecular orbital (LUMO) level of PIDTSCDTS was estimated to be −3.66 eV based on its HOMO energy level and the corresponding optical bandgap. The LUMO energy levels of the two dopants, $FeCl_3$ and $AuCl_3$, were measured to be −4.97 eV and −5.76 eV, respectively, in acetonitrile (Fig. 1d). The incorporation of the electron-sufficient IDT and CDT moieties resulted in a high HOMO energy level of PIDTSCDTS, facilitating p-doping by $AuCl_3$ and $FeCl_3$.

Density functional theory (DFT) calculations were performed at the B3LYP/6-31G*(d,p) level to study the electronic structure and energy minimum geometry of the polymer. For simplicity, a model dimer structure with side chains truncated to methyl groups was used in the calculations. The calculated structure shows a pronounced chain planarity, suggesting a good agreement with our molecular design strategy. Although a small torsional angle of 14° between the IDT and CDT moieties was calculated in the gas phase, the planar chain conformation in the solid state could be further enhanced, leading to aggregation-induced planarization *via* the strong π–π stacking interchain interactions. As shown in Fig. S2 (ESI†), the HOMO and LUMO are delocalized over the entire conjugated backbone, and thus efficient delocalization of the charge carriers and their transport in the doped states are expected.

Molecular doping was investigated in detail using three doping methods: SqD, MxD, and HyD.[27–31] For SqD, the dopant solution in a semi-orthogonal solvent (acetonitrile) at various concentrations (0.01–100 mM) was spin-coated on top of pre-coated pristine PIDTSCDTS (from 8 mg mL$^{-1}$ in chloroform) films on glass substrates; the polymer film was swelled to allow the dopants to penetrate the polymer matrix without washing out the underlying polymer films. For the MxD process, we first prepared a dopant solution in tetrahydrofuran by changing the dopant concentration (5–50 mM); the dopant solution was then mixed with a polymer solution (in chloroform) at different mixing ratios and spin-coated onto glass substrates. For HyD, the SqD and MxD methods were combined. The films were first fabricated using MxD, and the MxD-polymer films were additionally doped using the SqD process. To optimize the doping conditions, the dopant concentrations were carefully controlled at both the MxD and HyD stages: the dopant solution concentration for the MxD stage was optimized at 0.05 mM of $AuCl_3$ and 0.5 mM of $FeCl_3$ because high concentrations of dopants result in aggregation and thus poor-quality films. Dopants at various concentrations (0.1–80 mM) were then overcoated on top of the MxD-cast film using the SqD method. More details of the doping procedures are described in the ESI.†

To investigate the generation of carriers (positive polarons/bipolarons), the UV-vis-NIR absorption spectra of the polymer films obtained using the three different doping methods were measured as a function of the dopant concentration. As displayed in Fig. 2(a, c and e), the bandgap absorption at 685 nm was gradually bleached upon doping with $AuCl_3$, and new mid-gap absorptions at ∼900 nm and over ∼1200 nm increased due to (bi)polaron generation.[32–36] With a further increase in the [$AuCl_3$], the peak at ∼900 nm (polaron generation) was saturated and then decreased, while the broad absorption at >1200 nm (bipolaron generation) continued to intensify concomitantly, which might be related to the polaron-to-bipolaron transition in heavily doped states.[37–39] The spectral change with doping was most pronounced in the HyD-films, and the MxD-films showed the weakest (bi)polaron absorptions, indicating

 

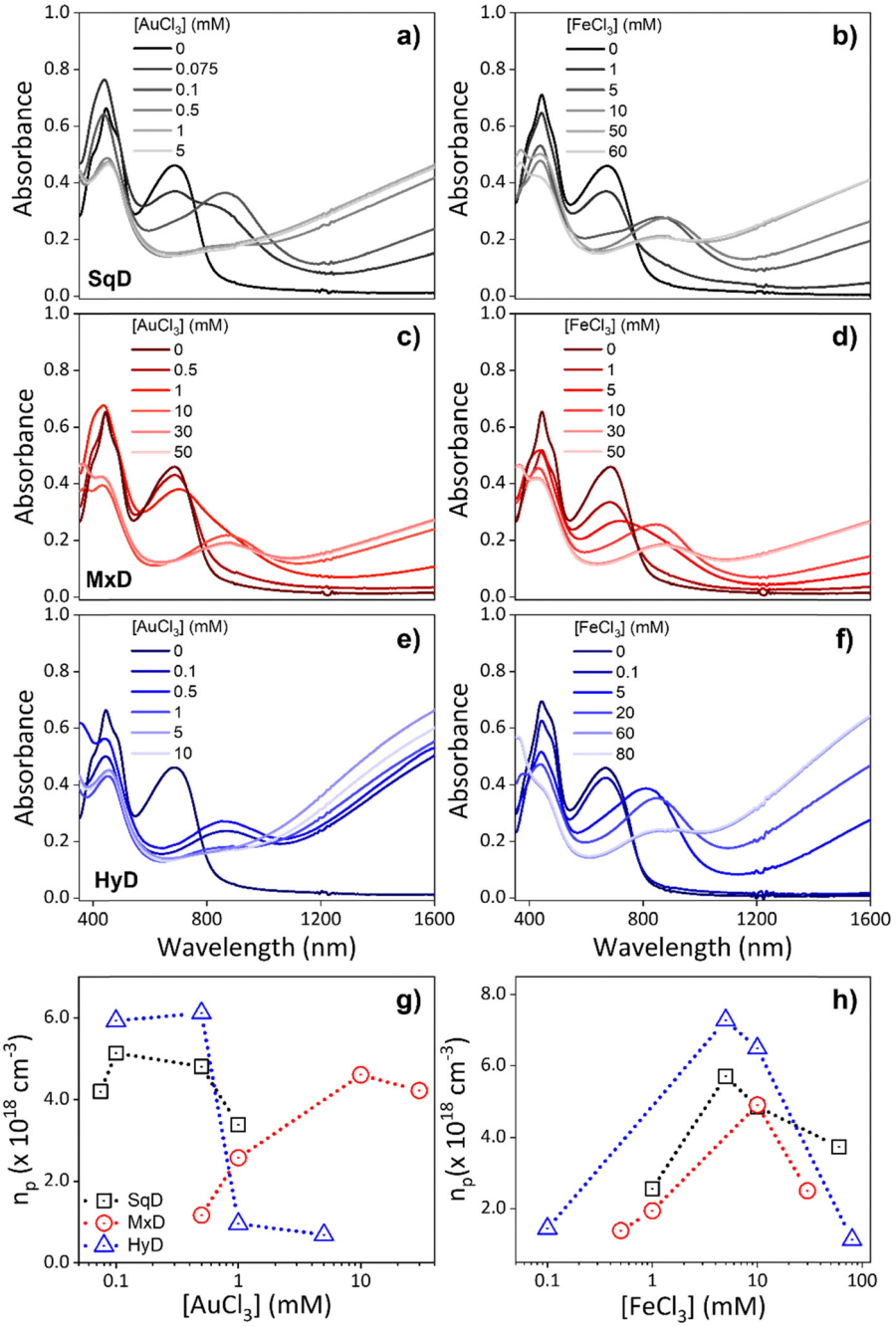


Fig. 2 (a–f) UV-vis-NIR spectra of PIDTSCDTS with variation of the doping concentration of (a, c and e) $AuCl_3$- and (b, d and f) $FeCl_3$-doped films *via* the (a and b) SqD, (c and d) MxD, and (e and f) HyD methods. (g and h) Polaron density of PIDTSCDTS doped using the SqD (black), MxD (red), and HyD (blue) method as a function of the (g) $AuCl_3$ and (h) $FeCl_3$ concentration. The dopant concentrations for HyD are those at the SqD stage ([$AuCl_3$] = 0.05 mM and [$FeCl_3$] = 0.5 mM are fixed in the MxD stage).

that charge generation is strongly dependent on the doping method. $FeCl_3$ also exhibited similar doping characteristics, as shown in Fig. 2(b, d and f). It is noteworthy that a higher [$FeCl_3$] is necessary to achieve similar doping level to $AuCl_3$, suggesting a lower doping efficiency of $FeCl_3$ compared with $AuCl_3$. The origin of the higher doping efficiency of $AuCl_3$ is its stronger oxidizing ability to accept up to 3 electrons by forming $Au^0$ nanoparticles. The details will be discussed in the following section.

The polaron concentration ($n_p$) as a function of the dopant concentration was analyzed using EPR measurements.[40] The doped polymer films were prepared in the same manner on a polyethylene terephthalate (PET) substrate. The polaron density was determined relative to 4-hydroxy-2,2,6,6-tetramethylpiperidin-1-oxyl (TEMPOL) used as a reference. In the SqD-PIDTSCDTS films, the polaron concentration initially increased from $2.09 \times 10^{17}$ to $5.53 \times 10^{18}$ $cm^{-3}$ with the increase in [$AuCl_3$] from

0 to 0.1 mM, respectively. After that, the EPR peak intensity gradually decreased with a further increase in [$AuCl_3$] to 1 mM, and the resulting polaron concentrations were calculated to be $4.80 \times 10^{18}$ and $3.38 \times 10^{18}$ $cm^{-3}$ at [$AuCl_3$] = 0.5 and 1 mM, respectively (Fig. 2g and Fig. S3, Table S1, ESI†). This must be related to the spin-active polaron to spinless bipolaron transition with increasing [$AuCl_3$], which is very consistent with the UV-vis-NIR spectral changes: the polaron peak at ~900 nm increases and decreases with a concomitant increase in the bipolaron absorption over ~1200 nm. In the case of MxD, a much higher dopant concentration was required to reach the maximum $n_p$ of $4.60 \times 10^{18}$ $cm^{-3}$ ([$AuCl_3$] = 10 mM), and the polaron-to-bipolaron transition was suppressed compared with the other two methods, indicating that MxD had the most inefficient doping among the three methods. For the HyD cases, the increase and decrease in $n_p$ were most prominent: the maximum $n_p$ of $6.11 \times 10^{18}$ $cm^{-3}$ was reached at [$AuCl_3$] = 0.5 mM, after which $n_p$ decreased drastically to $9.50 \times 10^{17}$ $cm^{-3}$ at [$AuCl_3$] = 1 mM. Together with the spectral changes in the UV-vis-NIR measurements, the decrease in $n_p$ with a concomitant increase in $\sigma$ (as discussed in the following section) suggests that the main charge carriers are spinless bipolarons in the heavily doped SqD- and HyD-PIDTSCDTS films. For $FeCl_3$ doping, the trend of polaron generation followed by bipolaron generation was similar to that for $AuCl_3$ doping (Fig. 2h and Fig. S3, ESI†), although a much higher [$FeCl_3$] was required to obtain analogous levels of polaron density.

The $\sigma$ values of $AuCl_3$- and $FeCl_3$-doped PIDTSCDTS were measured using the four-point probe method (Fig. 3a, Table 1 and Table S2, ESI†). On sequentially doping the polymer with [$AuCl_3$] = 0.01, 0.1, and 0.5 mM, the $\sigma$ increased from $1.3 \times 10^{-6}$ to 0.1, 55 and 135 S $cm^{-1}$ and the further increase of [$AuCl_3$] up to 1 mM gave the maximum conductivity ($\sigma_{max}$) of 272 S $cm^{-1}$. By contrast, doping *via* MxD only obtained the highest electrical conductivity of 10.1 S $cm^{-1}$ at [$AuCl_3$] = 30 mM. For the HyD method, after mixing the polymer solution with 0.05 mM of $AuCl_3$, the films were overcoated with [$AuCl_3$] = 0.1–30 mM, incurring the maximum $\sigma$ = 466 S $cm^{-1}$ at 5 mM $AuCl_3$. With an increasing dopant concentration, the $\sigma$ values increased regardless of the dopant or doping method, but to different extents. As mentioned above, the highest $\sigma$ = 466 S $cm^{-1}$ for the HyD-$AuCl_3$ films was significantly higher than the $\sigma_{max}$ value for the SqD and MxD films (272 and 10.1 S $cm^{-1}$ at [$AuCl_3$] = 1 and 30 mM, respectively). Similar results were obtained by doping PIDTSCDTS with $FeCl_3$. The $\sigma_{max}$ values of 250, 9.1, and 551 S $cm^{-1}$ were obtained *via* SqD, MxD and HyD, but at much higher [$FeCl_3$] values of 60, 30, and 80 mM, respectively.

Depending on the doping method, we extracted the $n$ values in the doped films using the Mott–Schottky equation (eqn (1))

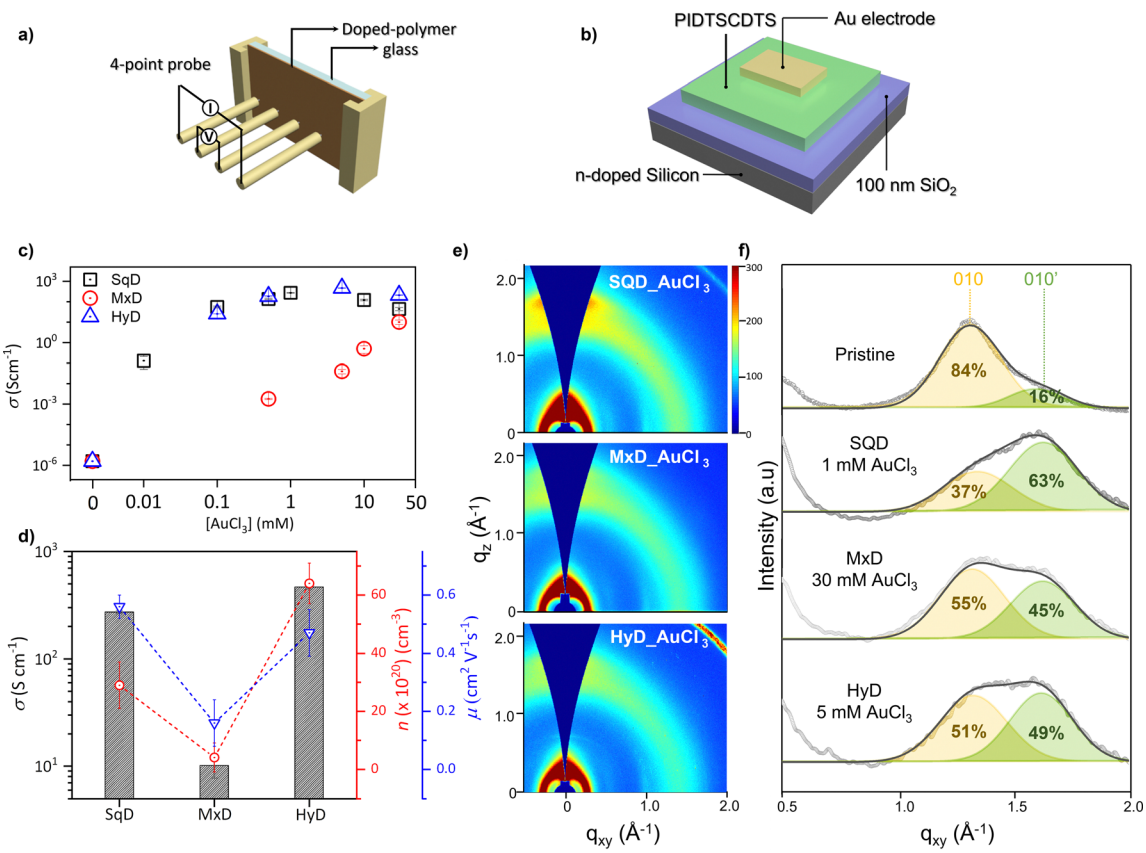


Fig. 3 Schematics of (a) the electrical conductivity setup and (b) the MIS capacitance measurement setup. (c) $\sigma$ values of $AuCl_3$-doped PIDTSCDTS films obtained *via* three doping methods as a function of the dopant concentration. (d) Comparison of $n$ and $\mu$ values at $\sigma_{max}$ for $AuCl_3$-doped PIDTSCDTS films *via* the three doping methods. (e) 2D-GIWAXS images and (f) corresponding out-of-plane line-cut profiles of PIDTSCDTS doped with $AuCl_3$ using three different methods.

 

Table 1 Summary of the TE properties of $AuCl_3$-doped polymer films

| Doping method | [$AuCl_3$] (mM) | $\sigma$ (S cm$^{-1}$) | $S$ ($\mu$V K$^{-1}$) | PF ($\mu$W m$^{-1}$ K$^{-2}$) |
|---|---|---|---|---|
| SqD | 0.01 | 0.13 ($\pm$0.08) | 442 ($\pm$57) | 2.5 ($\pm$0.3) |
| | 0.1 | 55 ($\pm$5) | 55 ($\pm$4) | 16 ($\pm$3) |
| | 0.5 | 135 ($\pm$8) | 22 ($\pm$2) | 6 ($\pm$1) |
| | 1 | 272 ($\pm$10) | 16 ($\pm$3) | 4.9 ($\pm$0.4) |
| | 10 | 121 ($\pm$10) | 5.4 ($\pm$0.8) | 0.15 ($\pm$0.04) |
| | 30 | 44 ($\pm$8) | 4.2 ($\pm$0.4) | 0.03 ($\pm$0.01) |
| MxD | 5 | 0.04 ($\pm$0.01) | 275 ($\pm$24) | 0.22 ($\pm$0.05) |
| | 10 | 0.5 ($\pm$0.2) | 85 ($\pm$5.6) | 0.70 ($\pm$0.1) |
| | 30 | 10.1 ($\pm$2.4) | 11 ($\pm$1) | 0.70 ($\pm$0.3) |
| | 50 | 6.6 ($\pm$2.1) | 6.4 ($\pm$0.9) | 0.04 ($\pm$0.02) |
| HyD | 0.1 | 25 ($\pm$0.1) | 102.6 ($\pm$25) | 26.8 ($\pm$1.2) |
| | 0.3 | 73 ($\pm$3.7) | 73.2 ($\pm$15) | 39.2 ($\pm$3.3) |
| | 0.5 | 184 ($\pm$12) | 33.0($\pm$5.1) | 21.0 ($\pm$3.3) |
| | 1 | 329 ($\pm$15) | 17.7 ($\pm$1.1) | 10.0 ($\pm$1.2) |
| | 5 | 466 ($\pm$20) | 14.0 ($\pm$1.1) | 9.2 ($\pm$1.2) |
| | 10 | 316 ($\pm$11) | 13.2 ($\pm$1.0) | 5.5 ($\pm$1.0) |
| | 30 | 209 ($\pm$10) | 7.3 ($\pm$1.0) | 1.1 ($\pm$0.2) |

*via* MIS capacitance measurements.[24,41] Fig. 3b shows a schematic of the MIS device structure with an architecture of n-doped silicon (resistivity ($\rho$) $< 0.002$ $\Omega$ cm)/100 nm $SiO_2$/doped polymer film/Au.

$$n = \frac{2}{q\varepsilon_0\varepsilon_r\left(\frac{\partial C_p^{-2}}{\partial V}\right)} \quad (1)$$

In eqn (1), $q$, $\varepsilon_0$, $\varepsilon_r$, $C_p$, and $V$ are the unit charge of the carriers, the permittivity of free space, the dielectric constant of the active layer, the specific capacitance of the device, and the applied voltage, respectively. The $C_p$–$V$ characteristics of the doped films are displayed in Fig. S4 (ESI†). The $\mu$ values were calculated from the $\sigma$ and $n$ values obtained from the four-point probe conductivity and MIS measurements. The $n$ and $\mu$ values at $\sigma_{max}$, depending on the doping method, are shown in Fig. 3d and Fig. S5 (ESI†). The $\mu$ value was the highest for the SqD films (0.56 cm$^2$ V$^{-1}$ s$^{-1}$ at [$AuCl_3$] = 1 mM) followed by the HyD films (0.47 cm$^2$ V$^{-1}$ s$^{-1}$ at [$AuCl_3$] = 5 mM) and the MxD films (0.16 cm$^2$ V$^{-1}$ s$^{-1}$ at [$AuCl_3$] = 30 mM). By contrast, the $n$ value at $\sigma_{max}$ was measured to be $2.9 \times 10^{21}$, $4.1 \times 10^{20}$, and $6.4 \times 10^{21}$ cm$^{-3}$ at [$AuCl_3$] = 1, 30, and 5 mM for the SqD-, MxD-, and HyD-PIDTSCDTS films, respectively. It is worth emphasizing that significantly higher $n$ values were determined for the HyD films than for the MxD (by one order of magnitude) and SqD films (>two times) with both $AuCl_3$ and $FeCl_3$ doping (Fig. 3d and Fig. S5, ESI†). This suggests that HyD effectively dopes both the crystalline and amorphous regions without a considerable decrease in the carrier mobility. The highest $n$ for HyD, despite its lowest $n_p$ at $\sigma_{max}$ (as calculated from the EPR data), again implies a major contribution of spinless bipolaronic species to $\sigma$. These correlations clearly suggest that the high $\sigma$ of the HyD films originates mainly from the abundant generation of charge carriers.

The tendency of $\mu$ was in good agreement with the 2D-GIWAXS measurements. We investigated the changes in the film morphology depending on the doping method at a given dopant concentration to show $\sigma_{max}$. The 2D-GIWAXS images and corresponding out-of-plane (OOP) line-cut profiles are shown in Fig. 3(e and f) and Fig. S6 (ESI†), and the resulting packing parameters are summarized in Table S3 (ESI†). Although PIDTSCDTS showed hump-shaped (100) and (010) scatterings, a dominant face-on orientation was observed with a strong (010) peak in the OOP direction. The broad (010) OOP scattering peak could be deconvoluted into two separate peaks [(010) at $q_z$ = 1.40 Å$^{-1}$ ($d$-spacing = 4.5 Å) and (010′) at $q_z$ = 1.71 Å$^{-1}$ ($d$-spacing = 3.7 Å)]. Loose and tighter π–π stackings were observed, and the resulting peak integration ratios are summarized in Table S3 (ESI†). When the pristine films were doped using the three different doping methods, the fraction of the (010′) peak changed from 16% (pristine) to 63%, 45%, and 49% (doped with $AuCl_3$) and 65%, 37%, and 62% (doped with $FeCl_3$) for the SqD-, MxD-, and HyD-films, respectively. Tighter interchain packing was observed in the order of SqD, HyD, and MxD films, which was consistent with the highest $\mu$ value for SqD. Thus, the weaker π–π stacking in the HyD films compared with the SqD films must be related to inclusion of the dopant in the crystalline regions during the MxD stage. Interestingly, distinct Au patterns at the edges of the 2D-GIWAXS images were also observed in the SqD and HyD films. This also supports the lower doping efficiency of MxD compared with that of the SqD and HyD methods.

The higher doping efficiency of HyD compared with the other two doping methods was further verified through X-ray photoelectron spectroscopy (XPS) measurements (at the dopant concentration yielding $\sigma_{max}$ for each doping method). First, the Fe 2p XPS peak was analyzed for the $FeCl_3$-doped films. When doping occurs, electrons are transferred from the polymer to the dopant [$FeCl_3 + e^- \rightarrow FeCl_2 + Cl^-$].[42–46] As a result, a broad Fe 2p signal originating from the $Fe^{2+}$ (reduced) and $Fe^{3+}$ (unreacted) species was observed. The relative doping efficiency can be estimated by comparing the Fe 2p peak integration ratio of $Fe^{2+}$ to $Fe^{3+}$, as shown in Fig. 4(a–c). The HyD-polymer films exhibited the most dominant $Fe^{2+}$ signal (67%) over $Fe^{3+}$ (32%), followed by SqD ($Fe^{2+}$ = 56%, $Fe^{3+}$ = 44%) and MxD ($Fe^{2+}$ = 31%, $Fe^{3+}$ = 69%). In the case of $AuCl_3$ doping, we observed four peaks at 84.3, 86.0, 88.0, and 89.7 eV, corresponding to $Au^0$ $4f_{7/2}$, $Au^{3+}$ $4f_{7/2}$, $Au^0$ $4f_{5/2}$, and $Au^{3+}$ $4f_{5/2}$, respectively (Fig. 4d).[43,47,48] In contrast to the $FeCl_3$ doping, $AuCl_4^-$ counter ions or $AuCl_3$ can be further reduced to $Au^0$ nanoparticles (Au NPs) by accepting three electrons from the polymer, which explains the origin of the efficient doping at low [$AuCl_3$], as discussed in the previous section. The $Au^0$ $4f_{7/2}$ and $Au^0$ $4f_{5/2}$ peaks confirm the formation of Au NPs, while the other two peaks, $Au^{3+}$ $4f_{7/2}$ and $4f_{5/2}$, originate from unreacted $AuCl_3$ dopant and/or counter anions in the form of $AuCl_4^-$ after doping.[43] The spin–orbit splitting by 3.6 eV with a $4f_{7/2}$ : $4f_{5/2}$ peak area ratio of 4 : 3 was observed for both neutral and oxidized peaks. The $Au^{3+}$ $4f_{7/2}$ and $f_{5/2}$ peaks were dominant in the MxD films, while the $Au^0$ 4f peaks were pronounced in the HyD and SqD polymer films, suggesting higher doping efficiencies for HyD and SqD compared with that of MxD. The XPS signal of Au NPs formation in the HyD- and SqD-films is very consistent with the Au scattering peaks in the GIWAXS measurements (see Fig. 3e). In addition, the higher

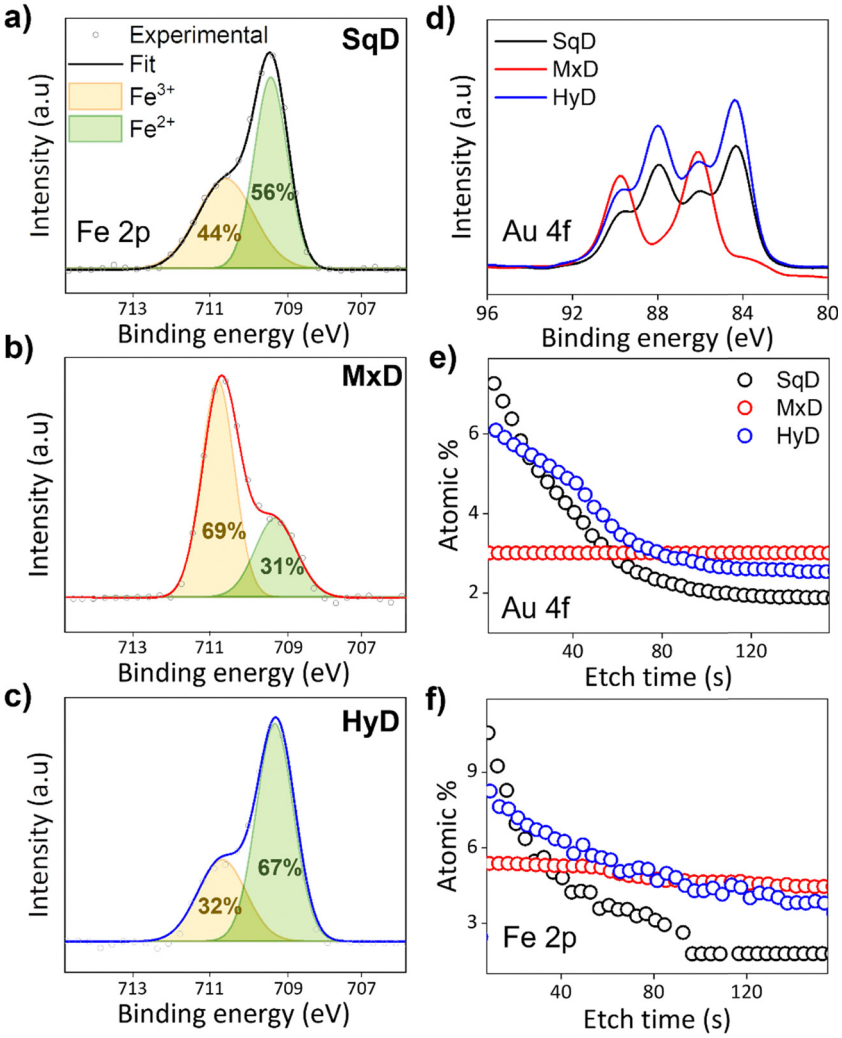


Fig. 4 XPS spectra of Fe 2p peaks of PIDTSCDTS doped *via* (a) SqD, (b) MxD, and (c) HyD using $FeCl_3$ and (d) Au 4f peaks of PIDTSCDTS doped *via* the three doping methods using $AuCl_3$. XPS depth profiles of (e) Au 4f and (f) Fe 2p peaks depending on the doping method.

doping ability of HyD was also confirmed by the peak shift of the S 2p signal: positively charged (bi)polaron generation along the polymer backbone increases its binding energy and induces a peak shift to a higher binding energy.[49–54] Upon doping with $AuCl_3$, larger S 2p peak shifts were measured for the SqD- and HyD-films than for the MxD-film: from 163.6 eV (pristine) to 164.5, 164.1, and 164.6 eV for the SqD-, MxD- and HyD-films, respectively (Fig. S7a, ESI†). The same trend was observed for the $FeCl_3$-doped PIDTSCDTS films (Fig. S7b, ESI†). Analysis of the XPS data for the Fe 2p, Au 4f, and S 2p signals clearly confirms that the HyD and SqD methods provide much more efficient doping than MxD, regardless of the dopant used, which is in good agreement with the UV-vis-NIR measurements.

We also measured the XPS depth profiles of the doped films using ion beam etching to determine the dopant distribution in the vertical direction. As shown in Fig. 4(e and f), a homogeneous distribution of dopants was observed in the MxD films, whereas the SqD and HyD films clearly showed a concentration gradient along the depth direction. Because of the intrinsic nature of SqD (where dopants penetrate from the surface into the polymer film), a larger concentration of the dopant stayed near the surface, and the dopant concentration gradually decreased in the vertical direction. The HyD films showed a similar trend, although the concentration gradient was much smaller than that of the SqD films because HyD combines both SqD and MxD. In SqD, the dopants mainly penetrate the less-crystalline/amorphous regions which can be mainly doped in this method. By contrast, HyD combines the MxD and SqD processes and thus dopes both the crystalline and amorphous regions, which improves the doping efficiency and homogeneity of the doped films. Furthermore, both the carrier concentration and the carrier transport ability (and resulting conductivity) can be enhanced using HyD, improving the structural connectivity and charge percolation by doping both the amorphous and crystalline domains. In HyD, the fine-adjustment of the MxD step is particularly important to suppress the phase separation of the host polymer and dopant molecules without destroying the crystalline interchain packing of the polymers.

To examine the TE properties of $AuCl_3$- and $FeCl_3$-doped PIDTSCDTS, $S$ values were measured using a homemade

 

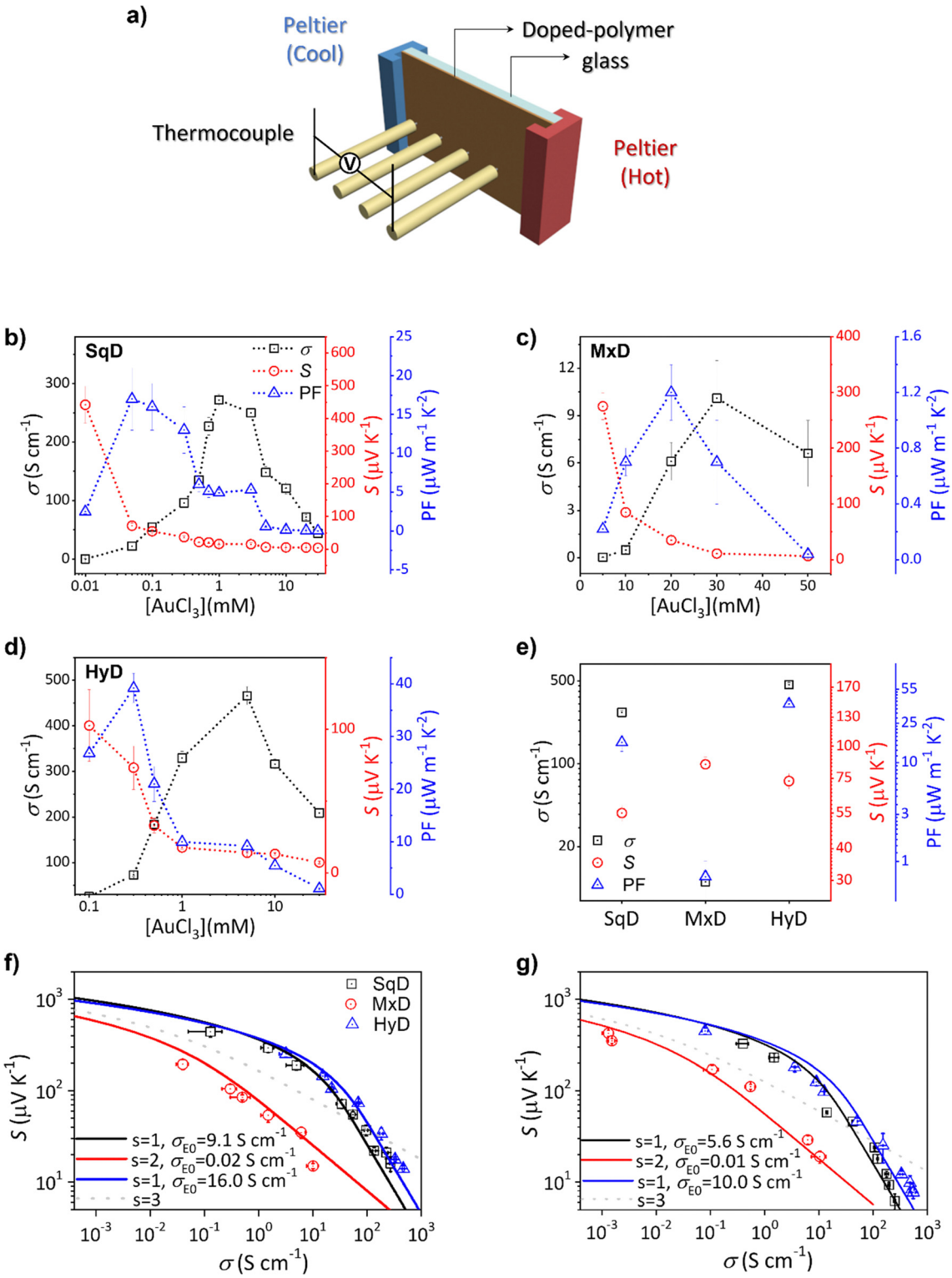


Fig. 5 (a) Schematic of the Seebeck coefficient measurement setup. (b–d)Thermoelectric characteristics of the PIDTSCDTS films doped with $AuCl_3$ using (b) SqD, (c) MxD, and (d) HyD. (e) Maximum $\sigma$, PF, and $S$ (at the maximum PF) for the $AuCl_3$-doped films. (f and g) $S$–$\sigma$ relationship analysis using the Kang–Snyder model for polymer films doped with (f) $AuCl_3$ and (g) $FeCl_3$. The solid lines show the fitting curves with $s = 1$ for the SqD and HyD films or $s = 2$ for the MxD films. The dotted line shows the calculated curve with $s = 3$ for comparison.

Peltier-based setup (Fig. 5a).[55] The $S$ values were determined by measuring the potential difference (thermovoltage) under a temperature gradient of 1–3 K under ambient conditions. Ten separate measurements were performed and the average values were plotted. The measured $\sigma$, $S$, and PF values are plotted in Fig. 5(b–e) and Fig. S8 (ESI†) and summarized in Table 1 and

Table S2 (ESI†). As we discussed above, the HyD films achieved a higher $\sigma$ owing to their markedly higher $n$ ($\sim 10^{21}$ cm$^{-3}$) despite their smaller $\mu$ than the SqD films at $\sigma_{max}$. The $S$ value decreased from 102.6 μV K$^{-1}$ at [$AuCl_3$] = 0.1 mM to 7.3 μV K$^{-1}$ at [$AuCl_3$] = 30 mM under HyD. The $\sigma$ and $S$ values showed a typical trade-off relationship for all the films doped using SqD, MxD, and HyD. By finely optimizing the dopant concentration, a maximum PF ($PF_{max}$) of 39.2 μW m$^{-1}$ K$^{-2}$ was obtained using HyD at [$AuCl_3$] = 0.3 mM, which was higher than the values obtained using the SqD and MxD methods (16 μW m$^{-1}$ K$^{-2}$ for SqD films and 0.7 μW m$^{-1}$ K$^{-2}$ for MxD films). Similarly, in the $FeCl_3$-doped films, the $PF_{max}$ for the HyD films was 11.4 μW m$^{-1}$ K$^{-2}$, while those of the SqD and MxD films were 9.0 and 0.57 μW m$^{-1}$ K$^{-2}$, respectively. This trend of a higher PF for the HyD films can be attributed to the significantly enhanced $\sigma$ with a mitigated $S$–$\sigma$ trade-off relation, which will be discussed in terms of the charge transport behavior in doped states, depending on the doping method.

The Kang–Snyder model was used to investigate the effect of the doping method on the charge carrier transport behavior in the doped polymer films. By fitting the experimental $S$–$\sigma$ values, the two essential factors of the transport parameter ($s$) and the transport coefficient ($\sigma_{E0}$) were determined (details are provided in the ESI†). The $s$ value is related to the charge-transport mechanism, and $\sigma_{E0}$ represents the charge-transport ability. Chemically doped organic semiconductors often show $S$–$\sigma$ characteristics that can be fitted with $s$ = 3, suggesting hopping transport of the charge carriers, which is limited by ionized impurity scattering.[28] Interestingly, the $S$–$\sigma$ curves of the SqD- and HyD-PIDTSCDTS films fit the calculated results well with $s$ = 1 (Fig. 5f and g), showing that $S \propto \sigma^{-1}$. This suggests the band-like carrier transport in the SqD and HyD films, which is mainly governed by acoustic phonon scattering.[56,57] The metal-like carrier transport behavior has been rarely reported except for PEDOT derivatives and very limited structures.[8,24,58] According to previous literature reports, band-like carrier transport ($s$ = 1) was observed in highly ordered polymer systems. It was emphasized that acoustic phonon scattering generally yields a higher carrier mobility than ionized-impurity scattering ($s$ = 3), yielding a higher $\sigma_{E0}$ in crystalline polymeric systems.[23] In addition, the $S$–$\sigma$ curve for MxD could be fitted well with $s$ = 2, which indicates that optical phonon scattering limits the charge transport.[59] The limitation of charge transport by optical phonon scattering has been theoretically reported to be dominant in lightly doped and low-crystalline semiconductors.[23,60–62]

In addition, $\sigma_{E0}$ also plays an important role in enhancing the PF.[63] Usually, the localized state within the ordered domains limits $\sigma_{E0}$, which can be overcome by improving the transport between crystalline regions. Based on our fitting results, the $\sigma_{E0}$ values followed the order HyD > SqD > MxD for both the $AuCl_3$- and $FeCl_3$-doped films. Specifically, in the $AuCl_3$-doped films, the $\sigma_{E0}$ values were determined to be 16.0 S cm$^{-1}$ for the HyD films and 9.1 S cm$^{-1}$ for the SqD films. With regard to the higher $\sigma_{E0}$ of the HyD-films, we hypothesize that the structural connectivity of ordered domains might be improved *via* HyD doping of both the amorphous and crystalline domains, resulting in enhancement of the charge percolation among the ordered domains. This behavior was also supported by the temperature-dependent $\sigma$ measurement in a low-temperature region (down to 150 K). In Fig. S9a and b (ESI†), the $\sigma$ values become constant as the temperature decreases below a certain temperature for the SqD- and HyD-films (with both $AuCl_3$ and $FeCl_3$ dopants), suggesting an insulator-to-metal transition in low-temperature regions. We plotted the reduced activation energy ($W(T) = d\ln[\sigma(T)]/d\ln(T)$) *versus* $T$ (the Zabrodskii plot).[24,64] As shown in Fig. S9c and d (ESI†), the SqD- and HyD-films with $AuCl_3$ exhibited a positive slope, indicating that the films have a metallic nature. However, the slope became smaller, and the $W(T)$ values remained almost constant for the MxD-films with $AuCl_3$. The $FeCl_3$-doped films also display the same trend. The temperature-dependent $\sigma$ values show good agreement with the fitting results based on the Kang–Snyder model. Consequently, an approximately two-fold higher $PF_{max}$ of 39.2 μW m$^{-1}$ K$^{-2}$ was achieved for HyD-PIDTSCDTS compared with that of SqD-PIDTSCDTS (16 μW m$^{-1}$ K$^{-2}$). Interestingly, both $\sigma$ and $S$ were higher for the HyD films than for the SqD films under the $PF_{max}$ condition. As discussed above, the higher $\sigma$ of HyD-PIDTSCDTS can be ascribed to the higher $n$ and $\sigma_{E0}$. Furthermore, the higher $\sigma_{E0}$ (carrier transport ability) of the HyD films is expected to weaken the trade-off relationship between the $\sigma$ and $S$ values by reducing the sacrifice of $S$ with increasing $\sigma$: the enhanced $\sigma_{E0}$ (with same $n$) increases the $\sigma$ but does not decrease the $S$ value (see eqn (S4) in the ESI†). Previous literature reports have also tried to decouple $\sigma$ and $S$ by blending polymers that have a small HOMO energy level offset or copolymerization. For example, Katz *et al.* reported that the introduction of poly(3-hexylthiothiophene (P3HTT) as an additive to P3HT films increased the $\sigma$ of the composites with slightly increased or constant $S$ values with the increase in the dopant concentration.[65] The small amount of P3HTT altered the density of states (DOS) distribution because of the difference in the energy levels of the two polymers. In addition, the authors suggested a possibility that it was also influenced by differences in the associations of the dopants with the polymers and dopant-induced interchain interactions.[66] By contrast, Gao *et al.* alleviated the $S$–$\sigma$ trade-off interrelation through the random copolymerization of two-dimensional (BDTTT-DPP) and one-dimensional (DPP-EDOT) monomers.[67] The crystallinity could be improved by the BDTTT-DPP unit, while the p-doping efficiency could be escalated by the DPP-EDOT unit, resulting in the simultaneous enhancement of $S$ and $\sigma$. Along with previous reports, our study may suggest another effective strategy to maximize the thermoelectric performance. It is noteworthy to emphasize that the synergistic effect of the electron-rich D–D′-type molecular design (having planar and extended conjugation with $sp^2$ alkenyl side chains) and the optimal HyD (for both amorphous and crystalline regions) successfully demonstrated metal-like carrier transport under degenerately doped conditions.

## 3. Conclusions

A new D–D′-type and electron-rich thermoelectric polymer (PIDTSCDTS) with extended π-conjugation was synthesized by

 

substituting $sp^2$ alkenyl side chains along the conjugated backbone. Its doping characteristics were studied in detail using three different doping methods (SqD, MxD, and HyD) with two Lewis acids ($AuCl_3$ and $FeCl_3$) as p-dopants. $AuCl_3$ induced efficient doping at lower dopant concentrations compared with $FeCl_3$ owing to its higher oxidizing ability by accepting up to three electrons. The HyD method achieved a significantly higher conductivity (up to $\sim$500 S $cm^{-1}$), which originated from degenerate doping (with $n$ up to $10^{21}$ $cm^{-3}$) in both the crystalline and amorphous regions (with facile polaron-to-bipolaron transitions) as well as a high $\sigma_{E0}$ (whilst maintaining semi-crystalline interchain packing). Distinct charge transport characteristics depending on the doping method were also studied by analyzing the $S$–$\sigma$ relationship based on the Kang–Snyder model. In contrast to the MxD polymer films, the SqD and HyD films showed metal-like carrier transport behavior, as the $S$–$\sigma$ curve could be fitted well with the transport parameter $s$ = 1. The synergistic contribution of the electron-rich D–D′-type design motif with extended π-conjugation and heavy doping *via* HyD without disrupting the semi-crystalline packing successfully demonstrated metal-like carrier transport under degenerately doped conditions. Moreover, the higher $\sigma_{E0}$ in the HyD films reduced the sacrifice of $S$ with increasing $\sigma$, which led to a higher $PF_{max}$ of $\sim$40 μW $m^{-1}$ $K^{-2}$ with simultaneous enhancement of the $\sigma$ and $S$ values compared with the SqD films (16 μW $m^{-1}$ $K^{-2}$). Degenerate doping and metal-like carrier transport whilst maximizing the $\sigma_{E0}$ (with low energetic disorder and a narrow density of states distribution in a doped state) need to be carefully considered for further improving the PF whilst mitigating the $S$–$\sigma$ trade-off relation.

## Author contributions

A. T., Y. L., and C. J. contributed equally to this work.

## Conflicts of interest

There are no conflicts to declare.

## Acknowledgements

This work was supported by the National Research Foundation (NRF) of Korea (2020M3H4A3081814, 2019R1A6A1A11044070, 2021R1A4A1030944 and 2021R1A2C2008325).

## References

1 G. H. Kim, L. Shao, K. Zhang and K. P. Pipe, *Nat. Mater.*, 2013, **12**, 719–723.
2 Y. Wang, C. Zhu, R. Pfattner, H. Yan, L. Jin, S. Chen, F. Molina-Lopez, F. Lissel, J. Liu, N. I. Rabiah, Z. Chen, J. W. Chung, C. Linder, M. F. Toney, B. Murmann and Z. Bao, *Sci. Adv.*, 2017, **3**, e1602076.
3 F. Zhang, Y. Zang, D. Huang, C. A. Di, X. Gao, H. Sirringhaus and D. Zhu, *Adv. Funct. Mater.*, 2015, **25**, 3004–3012.
4 V. Vijayakumar, E. Zaborova, L. Biniek, H. Zeng, L. Herrmann, A. Carvalho, O. Boyron, N. Leclerc and M. Brinkmann, *ACS Appl. Mater. Interfaces*, 2019, **11**, 4942–4953.
5 A. R. Chew, R. Ghosh, Z. Shang, F. C. Spano and A. Salleo, *J. Phys. Chem. Lett.*, 2017, **8**, 4974–4980.
6 Z. Y. Xu, R. Z. Wang and C. Yang, *Energy*, 2019, **176**, 1037–1043.
7 S. Hwang, W. J. Potscavage, R. Nakamichi and C. Adachi, *Org. Electron.*, 2016, **31**, 31–40.
8 C. J. Boyle, M. Upadhyaya, P. Wang, L. A. Renna, M. Lu-Díaz, S. Pyo Jeong, N. Hight-Huf, L. Korugic-Karasz, M. D. Barnes, Z. Aksamija and D. Venkataraman, *Nat. Commun.*, 2019, **10**, 1–10.
9 O. Bubnova, Z. U. Khan, A. Malti, S. Braun, M. Fahlman, M. Berggren and X. Crispin, *Nat. Mater.*, 2011, **10**, 429–433.
10 Q. Zhang, Y. Sun, W. Xu and D. Zhu, *Adv. Mater.*, 2014, **26**, 6829–6851.
11 S. J. Wang, M. Panhans, I. Lashkov, H. Kleemann, F. Caglieris, D. Becker-Koch, J. Vahland, E. Guo, S. Huang, Y. Krupskaya, Y. Vaynzof, B. Büchner, F. Ortmann and K. Leo, *Sci. Adv.*, 2022, **8**, 9264.
12 Y. Sun, P. Sheng, C. Di, F. Jiao, W. Xu, D. Qiu and D. Zhu, *Adv. Mater.*, 2012, **24**, 932–937.
13 J. Sun, M. L. Yeh, B. J. Jung, B. Zhang, J. Feser, A. Majumdar and H. E. Katz, *Macromolecules*, 2010, **43**, 2897–2903.
14 J. Liu, L. Qiu, G. Portale, M. Koopmans, G. ten Brink, J. C. Hummelen and L. J. A. Koster, *Adv. Mater.*, 2017, **29**, 1701641.
15 G. Zuo, X. Liu, M. Fahlman and M. Kemerink, *Adv. Funct. Mater.*, 2018, **28**, 1703280.
16 M. Schwarze, C. Gaul, R. Scholz, F. Bussolotti, A. Hofacker, K. S. Schellhammer, B. Nell, B. D. Naab, Z. Bao, D. Spoltore, K. Vandewal, J. Widmer, S. Kera, N. Ueno, F. Ortmann and K. Leo, *Nat. Mater.*, 2019, **18**, 242–248.
17 I. E. Jacobs, C. Cendra, T. F. Harrelson, Z. I. Bedolla Valdez, R. Faller, A. Salleo and A. J. Moulé, *Mater. Horizons*, 2018, **5**, 655–660.
18 D. Scheunemann, E. Järsvall, J. Liu, D. Beretta, S. Fabiano, M. Caironi, M. Kemerink and C. Müller, *Chem. Phys. Rev.*, 2022, **3**, 021309.
19 H. Abdalla, G. Zuo and M. Kemerink, *Phys. Rev. B*, 2017, **96**, 241202.
20 D. T. Duong, C. Wang, E. Antono, M. F. Toney and A. Salleo, *Org. Electron.*, 2013, **14**, 1330–1336.
21 O. Bubnova, Z. U. Khan, H. Wang, S. Braun, D. R. Evans, M. Fabretto, P. Hojati-Talemi, D. Dagnelund, J. B. Arlin, Y. H. Geerts, S. Desbief, D. W. Breiby, J. W. Andreasen, R. Lazzaroni, W. M. Chen, I. Zozoulenko, M. Fahlman, P. J. Murphy, M. Berggren and X. Crispin, *Nat. Mater.*, 2013, **13**, 190–194.
22 T. S. Lee, S. Bin Lee, D. Y. Choi, E. H. Suh, T. K. An, Y. J. Jeong, J. Jang and Y. H. Kim, *Macromol. Res.*, 2022, **29**, 887–894.
23 S. Dongmin Kang and G. Jeffrey Snyder, *Nat. Mater.*, 2016, **16**, 252–257.
24 Y. Lee, J. Park, J. Son, H. Young Woo, J. Kwak, Y. Lee, J. Son, H. Y. Woo, J. Park and J. Kwak, *Adv. Funct. Mater.*, 2021, **31**, 2006900.

25 J. Lee, J. Kim, T. L. Nguyen, M. Kim, J. Park, Y. Lee, S. Hwang, Y. W. Kwon, J. Kwak and H. Y. Woo, *Macromolecules*, 2018, **51**, 3360–3368.
26 A. Tripathi, B. E. Seo, M. J. Kim, Y. Lee, S. Lee, S. E. Yoon, U. J. Kim, Y. W. Kwon, H. Seo, K. Kwak, J. H. Kim and H. Y. Woo, *Adv. Electron. Mater.*, 2022, 2200456.
27 S. E. Yoon, Y. Kang, G. G. Jeon, D. Jeon, S. Y. Lee, S. J. Ko, T. Kim, H. Seo, B. G. Kim and J. H. Kim, *Adv. Funct. Mater.*, 2020, **30**, 2004598.
28 S. Lee, S. Kim, A. Pathak, A. Tripathi, T. Qiao, Y. Lee, H. Lee and H. Y. Woo, *Macromol. Res.*, 2020, **28**, 531–552.
29 A. Tripathi, Y. Lee, S. Lee and H. Y. Woo, *J. Mater. Chem. C*, 2022, **10**, 6114–6140.
30 S. N. Patel, A. M. Glaudell, D. Kiefer and M. L. Chabinyc, *ACS Macro Lett.*, 2016, **5**, 268–272.
31 S. E. Yoon, J. M. Han, B. E. Seo, S. W. Kim, O. P. Kwon, B. G. Kim and J. H. Kim, *Org. Electron.*, 2021, **90**, 106061.
32 J. Yamamoto and Y. Furukawa, *J. Phys. Chem. B*, 2015, **119**, 4788–4794.
33 E. Hyun Suh, J. Gyu Oh, J. Jung, S. Hoon Noh, T. Seong Lee and J. Jang, *Adv. Energy Mater.*, 2020, **10**, 2002521.
34 J. L. Bredas and G. B. Street, *Acc. Chem. Res.*, 1985, **18**, 309–315.
35 M. B. Qarai, R. Ghosh and F. C. Spano, *J. Phys. Chem. C*, 2021, **125**, 24487–24497.
36 C. Enengl, S. Enengl, S. Pluczyk, M. Havlicek, M. Lapkowski, H. Neugebauer and E. Ehrenfreund, *ChemPhysChem*, 2016, **17**, 3836–3844.
37 I. Salzmann, G. Heimel, M. Oehzelt, S. Winkler and N. Koch, *Acc. Chem. Res.*, 2016, **49**, 370–378.
38 Z. Liang, H. H. Choi, X. Luo, T. Liu, A. Abtahi, U. S. Ramasamy, J. A. Hitron, K. N. Baustert, J. L. Hempel, A. M. Boehm, A. Ansary, D. R. Strachan, J. Mei, C. Risko, V. Podzorov and K. R. Graham, *Nat. Mater.*, 2021, **20**, 518–524.
39 S. Hwang, W. J. Potscavage, Y. S. Yang, I. S. Park, T. Matsushima and C. Adachi, *Phys. Chem. Chem. Phys.*, 2016, **18**, 29199–29207.
40 Y. Harima, T. Eguchi, K. Yamashita, K. Kojima and M. Shiotani, *Synth. Met.*, 1999, **105**, 121–128.
41 H. Guo, C. Y. Yang, X. Zhang, A. Motta, K. Feng, Y. Xia, Y. Shi, Z. Wu, K. Yang, J. Chen, Q. Liao, Y. Tang, H. Sun, H. Y. Woo, S. Fabiano, A. Facchetti and X. Guo, *Nature*, 2021, **599**, 67–73.
42 Y. Li, T. Sritharan, S. Zhang, X. He, Y. Liu and T. Chen, *Appl. Phys. Lett.*, 2008, **92**, 132908.
43 Y. H. Kang, S. J. Ko, M. H. Lee, Y. K. Lee, B. J. Kim and S. Y. Cho, *Nano Energy*, 2021, **82**, 105681.
44 B. Yu, M. Li, J. Wang, Z. Hu, X. Liu, Y. Zhu and X. Zhao, *Thin Solid Films*, 2012, **520**, 4089–4091.
45 X. Yuan, L. Shi, J. Zhao, S. Zhou, Y. Li, C. Xie and J. Guo, *J. Alloys Compd.*, 2017, **708**, 93–98.
46 K. K. Bharathi, G. Ramesh, L. N. Patro, N. R. C. Raju and D. K. Kim, *Mater. Res. Bull.*, 2015, **62**, 5–10.
47 M. P. Casaletto, A. Longo, A. Martorana, A. Prestianni and A. M. Venezia, *Surf. Interface Anal.*, 2006, **38**, 215–218.
48 C. Jin, An, Y. Hun Kang, C. Lee, S. Yun Cho, C. J. An, Y. H. Kang, C. Lee and S. Y. Cho, *Adv. Funct. Mater.*, 2018, **28**, 1800532.
49 J. L. Jenkins, P. A. Lee, K. W. Nebesny and E. L. Ratcliff, *J. Mater. Chem. A*, 2014, **2**, 19221–19231.
50 J. Zekonyte and T. Polcar, *ACS Appl. Mater. Interfaces*, 2015, **7**, 21056–21064.
51 M. I. Nandasiri, L. E. Camacho-Forero, A. M. Schwarz, V. Shutthanandan, S. Thevuthasan, P. B. Balbuena, K. T. Mueller and V. Murugesan, *Chem. Mater.*, 2017, **29**, 4728–4737.
52 C. Du, P. Li, F. Yang, G. Cheng, S. Chen and W. Luo, *ACS Appl. Mater. Interfaces*, 2018, **10**, 753–761.
53 L. Qie, W. Chen, X. Xiong, C. Hu, F. Zou, P. Hu and Y. Huang, *Adv. Sci.*, 2015, **2**, 1500195.
54 K. H. Tu, Y. Wang, Y. Kiyota, T. Iwahashi, Y. Ouchi, T. Mori and T. Michinobu, *Org. Electron.*, 2020, **87**, 105978.
55 H. Bark, J. Lee, H. Lim, H. Y. Koo, W. Lee and H. Lee, *ACS Appl. Mater. Interfaces*, 2016, **8**, 31617–31624.
56 L. Tang, M. Long, D. Wang and Z. Shuai, *Sci. China, Ser. B: Chem.*, 2009, **52**, 1646–1652.
57 B. Xu, J. Yin and Z. Liu, *Phonon Scattering and Electron Transport in Single Wall Carbon Nanotube*, InTech, 2013.
58 K. Kang, S. Schott, D. Venkateshvaran, K. Broch, G. Schweicher, D. Harkin, C. Jellett, C. B. Nielsen, I. McCulloch and H. Sirringhaus, *Mater. Today Phys.*, 2019, **8**, 112–122.
59 T. Mei, H. Wang, K. Du, X. Dai, W. Zhang, R. Liu and S. J. Chua, *Nanophotonics*, 2020, **9**, 4287–4293.
60 J. Cao, J. D. Querales-Flores, A. R. Murphy, S. Fahy and I. Savić, *Phys. Rev. B*, 2018, **98**, 205202.
61 D. Wang, W. Shi, J. Chen, J. Xi and Z. Shuai, *Phys. Chem. Chem. Phys.*, 2012, **14**, 16505–16520.
62 S. Fratini, M. Nikolka, A. Salleo, G. Schweicher and H. Sirringhaus, *Nat. Mater.*, 2020, **19**, 491–502.
63 G. J. Snyder, A. H. Snyder, M. Wood, R. Gurunathan, B. H. Snyder and C. Niu, *Adv. Mater.*, 2020, **32**, 2001537.
64 X. Wang, X. Zhang, L. Sun, D. Lee, S. Lee, M. Wang, J. Zhao, Y. Shao-Horn, M. Dinca, T. Palacios and K. K. Gleason, *Sci. Adv.*, 2018, **4**(9), eaat5780, DOI: **10.1126/sciadv.aat5780**.
65 J. Sun, M. L. Yeh, B. J. Jung, B. Zhang, J. Feser, A. Majumdar and H. E. Katz, *Macromolecules*, 2010, **43**, 2897–2903.
66 H. Li, E. Plunkett, Z. Cai, B. Qiu, T. Wei, H. Chen, S. M. Thon, D. H. Reich, L. Chen and H. E. Katz, *Adv. Electron. Mater.*, 2019, **5**, 1800618.
67 G. Cao, B. Li, Y. Wu, Z. Ren, X. Nie, J. Yang, J. Wu, H. Xin, L. Wang and C. Gao, *Compos. Commun.*, 2022, **33**, 101218.

 